



Cite this: *Nanoscale*, 2015, 7, 17450

## Synthesis and characterization of barium silicide (BaSi<sub>2</sub>) nanowire arrays for potential solar applications†

Ankit Pokhrel, Leith Samad, Fei Meng and Song Jin\*

In order to utilize nanostructured materials for potential solar and other energy-harvesting applications, scalable synthetic techniques for these materials must be developed. Herein we use a vapor phase conversion approach to synthesize nanowire (NW) arrays of semiconducting barium silicide (BaSi<sub>2</sub>) in high yield for the first time for potential solar applications. Dense arrays of silicon NWs obtained by metal-assisted chemical etching were converted to single-crystalline BaSi<sub>2</sub> NW arrays by reacting with Ba vapor at about 930 °C. Structural characterization by X-ray diffraction and high-resolution transmission electron microscopy confirm that the converted NWs are single-crystalline BaSi<sub>2</sub>. The optimal conversion reaction conditions allow the phase-pure synthesis of BaSi<sub>2</sub> NWs that maintain the original NW morphology, and tuning the reaction parameters led to a controllable synthesis of BaSi<sub>2</sub> films on silicon substrates. The optical bandgap and electrochemical measurements of these BaSi<sub>2</sub> NWs reveal a bandgap and carrier concentrations comparable to previously reported values for BaSi<sub>2</sub> thin films.

Received 4th June 2015,  
Accepted 21st September 2015

DOI: 10.1039/c5nr03668b

www.rsc.org/nanoscale

### Introduction

BaSi<sub>2</sub> is an earth-abundant semiconductor possessing several key physical properties that make it an ideal material for solar cell applications. It has direct and indirect bandgaps of about 1.1 and 1.3 eV, respectively, a high light absorption coefficient reaching 10<sup>5</sup> cm<sup>-1</sup>, a high carrier mobility (1000 cm<sup>2</sup> V<sup>-1</sup> s<sup>-1</sup>), and a long carrier lifetime.<sup>1–3</sup> Besides these attractive physical properties, Si and Ba are the 2<sup>nd</sup> and 14<sup>th</sup> most abundant elements in Earth's crust, respectively, which makes BaSi<sub>2</sub> a promising material for low-cost solar cells. Despite such attractive attributes, there are only limited studies of BaSi<sub>2</sub> as a potential solar material partially due to its reactivity with moisture, which makes it inconvenient for these studies.<sup>3–5</sup> Moreover, thin film morphology allows facile integration of the material into a practical solar device and can potentially reduce fabrication issues related with the material. Thin films of BaSi<sub>2</sub> have been synthesized using processes such as molecular beam epitaxy (MBE) and other expensive growth techniques that have higher manufacturing cost,<sup>1,4</sup> making the development of alternative and facile synthesis routes desirable for practical applications. In addition to the thin films, nanowires (NWs) of BaSi<sub>2</sub> can potentially enhance solar per-

formance by effectively absorbing incident sunlight along the long axial direction and efficiently separating the photogenerated carriers in the short radial direction.<sup>6,7</sup> Moreover, NW arrays directly synthesized on an underlying substrate can potentially take advantage of both the improved performance due to their nanoscale morphology and the reduced fabrication costs due to their thin film-like morphology. Additionally, individual single-crystalline NWs can also serve as an attractive platform to study key physical properties that are crucial for potentially using this material for solar applications.<sup>8,9</sup>

However, there has been no report on the synthesis of BaSi<sub>2</sub> NWs. The rational synthesis of BaSi<sub>2</sub> NWs can be difficult due to their complex phase behavior. Five different thermodynamically stable phases (Ba<sub>2</sub>Si, Ba<sub>5</sub>Si<sub>3</sub>, BaSi, Ba<sub>3</sub>Si<sub>4</sub>, and BaSi<sub>2</sub>) are present in the Ba–Si binary phase diagram,<sup>10</sup> and selectively synthesizing BaSi<sub>2</sub> phase can be challenging. Several techniques have been developed for the direct growth of a variety of free-standing silicide NWs,<sup>11</sup> including FeSi,<sup>12</sup> CoSi,<sup>13,14</sup> Fe<sub>1-x</sub>Co<sub>x</sub>Si,<sup>15,16</sup> MnSi,<sup>17,18</sup> MnSi<sub>1.8</sub>,<sup>19</sup> α-Mn<sub>5</sub>Si<sub>3</sub>,<sup>18</sup> β-Mn<sub>5</sub>Si<sub>3</sub>,<sup>18</sup> Mn<sub>3</sub>Si,<sup>18</sup> CrSi<sub>2</sub>,<sup>20</sup> Ni<sub>2</sub>Si,<sup>21</sup> and Ni<sub>3</sub>Si<sup>22</sup> NWs. Out of the various approaches, silicidation of Si NW provides a relatively simple route to synthesize silicide nanostructures in reasonable yield. This approach was first reported in the Ni–Si system, where a Si NW was covered with a thermally evaporated Ni thin film and subsequently annealed to produce single-crystalline NiSi NWs *via* a solid-state reaction.<sup>23</sup> This approach has been used to synthesize other Ni–Si phases<sup>24–27</sup> and extended to other metals, such as Fe to form FeSi, α-FeSi<sub>2</sub>,

Department of Chemistry, University of Wisconsin – Madison, 1101 University Avenue, Madison, Wisconsin 53706, USA. E-mail: jin@chem.wisc.edu

†Electronic supplementary information (ESI) available. See DOI: 10.1039/c5nr03668b



and  $\beta$ -FeSi<sub>2</sub> NWs;<sup>28</sup> Pt resulting in PtSi NWs;<sup>29–31</sup> Co to form CoSi<sub>2</sub> NWs;<sup>32</sup> and Mn to produce Mn<sub>5</sub>Si<sub>3</sub> NWs<sup>33</sup> and MnSi NWs.<sup>34,35</sup> However, the NWs produced in this way are not always single crystalline.

Silicidation of Si NWs has usually been considered a low-throughput method for the production of silicide NWs, but recent silicidation work on NW array conversion shows that the silicidation approach can be a facile way to produce high-density silicide NW arrays.<sup>36–40</sup> Moreover, this technique also allows direct integration of the NWs to the underlying film on silicon substrates, therefore making them easier to integrate into thin-film devices. In this scheme, dense Si NW arrays, usually prepared by electrochemical etching of Si wafer, are used as the initial nanostructures for the conversion, and the metal source is then introduced, followed by high-temperature annealing to form silicide NW arrays.<sup>36–40</sup> Compared with the silicidation of individual NWs, this method can form wires in higher density, and controlling the concentration of the precursor allows for the tuning of the phase and structure of the converted silicide nanostructures. Moreover, as an alkaline earth metal, Ba is the most reactive metal among the metals involved in metal silicide NWs reported so far, and its reactivity and high vapor pressure could be directly utilized in the silicidation approach to form high-density BaSi<sub>2</sub> NW arrays. Therefore, by using a different precursor introduction approach as compared to previous works<sup>37–40</sup> and taking advantage of the high reactivity of Ba, we have extended the vapor phase conversion approach initially developed to synthesize higher manganese silicide (HMS) NWs, to convert silicon NW arrays into single-crystalline BaSi<sub>2</sub> NW arrays in high yield for the first time. Furthermore, by tuning the reaction parameters away from the ideal NW synthesis conditions, we can controllably synthesize BaSi<sub>2</sub> films on silicon substrates. The NWs converted under optimized conditions were confirmed to be single-crystalline BaSi<sub>2</sub> by various structural characterization techniques, and their properties were studied by optical and electrochemical techniques. The optical bandgap measurements show that the NWs have direct and indirect bandgaps of 1.06 and 1.27 eV, respectively, and the electrochemical measurements suggest that the converted NWs are n-type with a carrier concentration of  $1 \times 10^{19} \text{ cm}^{-3}$ .

## Experimental section

All chemicals and reagents were purchased from Sigma-Aldrich unless otherwise noted.

### Preparation of Si nanowire arrays

The Si NW arrays were prepared using a metal-assisted chemical etching method reported previously.<sup>41</sup> Briefly, degenerately doped Si (100) substrates, roughly 1 cm by 3 cm in size, were sonicated at 100% power in ethanol, isopropyl alcohol, and acetone for 5 min each to remove any surface residues. The chip was then rinsed with deionized water and dried with N<sub>2</sub> gas. After the native oxide layer on the Si surface was etched

away using buffered HF (buffered HF improved, Transene Inc.), the Si chip was placed into an etching solution of 4.8 M HF and 0.02 M AgNO<sub>3</sub> in a polyethylene beaker and placed in an oven at 50 °C for 1 h. The etched chip was then soaked in 8 M HNO<sub>3</sub> solution for 1 h to remove the Ag residue, vigorously rinsed with deionized water, and dried with N<sub>2</sub>.

### Vapor phase conversion synthesis of BaSi<sub>2</sub> nanowire arrays and thin films

Successful vapor phase conversion synthesis of BaSi<sub>2</sub> NWs and thin films was carried out inside a home-built CVD setup using a Lindberg Blue tube furnace, as shown in Fig. 1. In a typical NW conversion reaction, ~58 mg of Ba beads (0.5–2.0 mm particle size, 99% trace metals basis) was weighed out in a 1 mL alumina boat (CoorsTek) inside a nitrogen-filled glovebox. The boat was then sealed in a 15 mL glass vial, taken out of the glovebox, and quickly transferred to the center of the CVD tube furnace in which the Si NWs were already placed approximately 4.5 cm downstream from the center of the furnace. The tube was then quickly sealed, evacuated to base pressure, pressurized to 700 Torr with 10 sccm He gas flow, heated to 1000 °C, and held for 2 h. Various substrates were located at different positions along the tube furnace, but the

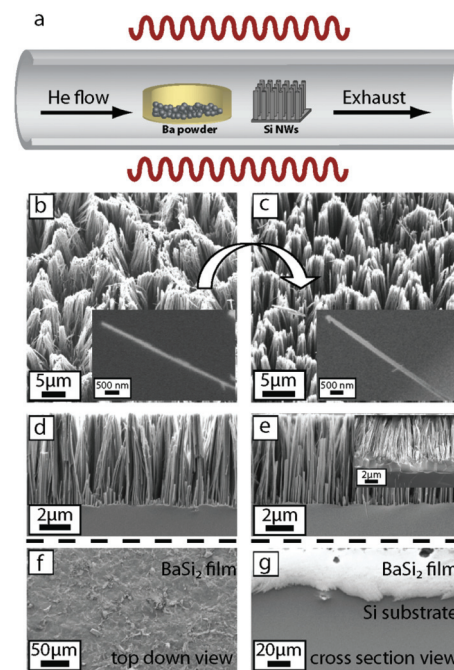


**Fig. 1** The conversion reaction set-up and the morphology of the starting and converted NWs and thin films. (a) A schematic showing the reaction setup; SEM micrographs (b–c) with a 30-degree tilt showing the morphology of (b) typical Si NW arrays before the conversion (inset shows an individual NW) and (c) the converted BaSi<sub>2</sub> NW arrays (inset shows an individual NW); (d–g) cross section SEMs showing the morphology of (d) Si NW arrays and (e) BaSi<sub>2</sub> NW arrays (inset shows the presence of BaSi<sub>2</sub> film between the NW and Si substrate); (f) top-down view and (g) cross-section SEM images of the converted BaSi<sub>2</sub> film on the Si chip.



optimal conversion was carried out when the Si NW was at approximately 930 °C and Ba beads were at 1000 °C at the center of the furnace. After reaction completion, the tube furnace was naturally cooled to room temperature under the flow of He gas, and the products were collected from the furnace for further characterization. The same synthesis procedure was used for the synthesis of BaSi<sub>2</sub> films, except the initial planar Si substrate was placed directly above the boat containing Ba beads at the center of the furnace, and the approximate temperature of both the beads and the chip was about 1000 °C.

### Structural characterization of BaSi<sub>2</sub> NW arrays and thin films

As-converted NWs and thin films were mounted onto metallic pucks using double-sided carbon tape and imaged with a LEO Supra 55 VP field emission scanning electron microscope (SEM). Powder X-ray diffraction (PXRD) data were acquired on the as-converted arrays using a Bruker D8 ADVANCE powder diffractometer using Cu K $\alpha$  radiation with a step size of 0.02 degrees. To perform energy dispersive spectroscopy (EDS) and transmission electron microscopy (TEM) on individual NWs, the converted NWs were scraped off the chip and dispersed in ethanol by sonication for ~30 min at 100% power. The suspension was drop-casted onto TEM grids (Ted Pella, lacey carbon type-A on 300 mesh copper grids) and dried with N<sub>2</sub>. EDS characterization was completed using a LEO30 SEM with a SiLi X-ray detector. High-resolution TEM (HRTEM) was carried out using a FEI TITAN aberration-corrected scanning transmission electron microscope (STEM) operated at 200 kV.

### Optical and electrochemical measurements

Optical bandgap measurements of the as-converted NWs were taken in reflectance mode using a Jasco V-570 UV-vis near-infrared (NIR) spectrometer with an integrating sphere. A baseline was collected using the bare silicon substrate and subsequently subtracted from the collected reflectance data to remove any signal from the underlying Si substrate. In order to perform electrochemical measurements, electrodes were fabricated using the as-converted NWs on silicon substrate by back-contacting copper wire with Ga-In eutectic ( $\geq 99.99\%$ ) to the underlying degenerately-doped Si substrate and then coating with silver paint (Ted Pella). The electrodes were then electrically isolated with an insulating epoxy and cured overnight. *J-V* measurements were taken in a two-electrode configuration using a platinum mesh counter electrode and an electrolyte consisting of 0.5 M KI and 0.05 M I<sub>2</sub> in anhydrous ethylene glycol. Electrochemical impedance spectroscopy (EIS) and Mott-Schottky measurements were performed in a solution of 0.1 M tetrabutylammonium perchlorate (TBAP) in anhydrous acetonitrile ( $\geq 99.0\%$ ) in a three-electrode configuration using a platinum mesh counter electrode and a Ag/AgCl reference electrode over the frequency range of 1 Hz to 5 MHz. All electrochemical measurements were performed using a Bio-Logic SP-200 potentiostat.

## Results and discussion

### Synthesis and characterization of BaSi<sub>2</sub> nanowire arrays and thin films

Successful vapor phase conversion of the Si NW arrays was performed inside a home-built CVD setup described previously<sup>17,18</sup> and shown in Fig. 1a. The major challenges in these conversion reactions include: (i) providing sufficient kinetics for the conversion while preserving the nanoscale morphology and (ii) controllably forming the BaSi<sub>2</sub> phase among the various Ba silicide phases (Ba<sub>2</sub>Si, Ba<sub>5</sub>Si<sub>3</sub>, BaSi, Ba<sub>3</sub>Si<sub>4</sub> and BaSi<sub>2</sub>). We used electrochemically etched dense and well-ordered Si NW arrays still attached to the Si substrate (Fig. 1b) with lengths of approximately 5  $\mu$ m (Fig. 1d) and average diameters of 123  $\pm$  34 nm (estimated from SEM images of 20 examined NWs) as the initial nanostructures. These NWs can be produced in reasonable yield. We have previously shown that using the Si substrate as a continuous source of Si in excess is crucial in the formation of the most silicon-rich metal silicide phase without other phase impurities.<sup>36</sup> As for the choice of precursor, we chose Ba beads because Ba has a relatively high vapor pressure of approximately 3.69 Torr at 1000 °C, which greatly facilitates the conversion reaction. We purposefully limited the amount of precursor in the system because our previous work<sup>36</sup> demonstrated that limiting the metal precursor in the reaction system also favors the formation of the silicon-rich silicide. Moreover, by simply using a Si chip instead of Si NWs as the initial nanostructure, we can controllably form BaSi<sub>2</sub> films on the silicon substrate. Therefore, by carefully controlling the reaction conditions in the optimized reactions described herein, we show that single-crystalline BaSi<sub>2</sub> NW arrays and thin films can be successfully obtained by converting Si NW arrays and Si chips, respectively.

The morphology of the as-converted NW arrays and films were examined using SEM (Fig. 1c, e, f and g). The converted NWs (Fig. 1c) appeared very similar to the initial nanostructures with lengths of approximately 5  $\mu$ m (Fig. 1e) and an average diameter of 130  $\pm$  52 nm (estimated from SEM images of 20 examined NWs). Some bundling of the nanostructures was observed in the final product, but for the most part, the converted nanostructures appeared vertical and separated. The converted films are approximately 10  $\mu$ m thick (Fig. 1g) and created a uniform layer covering the entire silicon substrate. Successful vapor phase conversion also requires the formation of the BaSi<sub>2</sub> phase without other major phase impurities. The PXRD patterns of the as-converted NW substrate and thin film (Fig. 2a) clearly show that most diffraction peaks can be successfully indexed to the BaSi<sub>2</sub> phase (PDF #71-2327) with very minor Ba<sub>3</sub>Si<sub>4</sub> and SiO<sub>2</sub> impurity phases. We also analyzed the elemental composition of individual NWs using EDS by scanning individual NWs for their elemental composition. A total of five NWs were analyzed, and for each NW, a spectrum scan was performed on multiple locations along the length of the NW. A typical EDS spectrum (Fig. 2b) on one of the analyzed NWs (shown in Fig. 2b inset) revealed the presence of Ba, Si, Al, Cu, O, and C. The C, Al, and Cu signals arise from the TEM



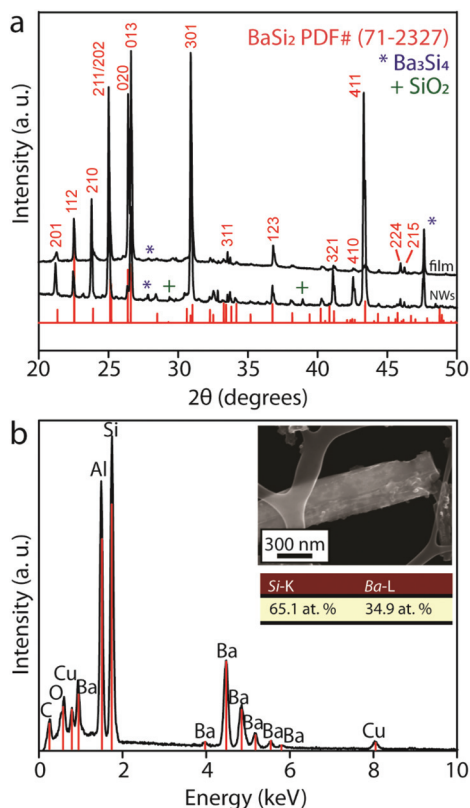


**Fig. 2** PXRD and EDS of the as-converted NWs and thin films. (a) PXRD of the as-converted film and NWs in comparison with the reference pattern for  $\text{BaSi}_2$  (PDF# 71-2327), with minor  $\text{Ba}_3\text{Si}_4$  and  $\text{SiO}_2$  indicated by \* and +, respectively; (b) EDS spectrum of a typical NW with quantification of the atomic percentage (shown in the inset) demonstrating the presence of Ba and Si and confirming the ratio of Ba : Si = 1 : 2 within the error of the EDS analysis.

grid and sample holder and were subtracted for the compositional calculations. The calculations showed that the elemental Ba : Si ratio in the converted nanostructures was approximately 1 : 2, very close to that of the  $\text{BaSi}_2$  phase.

### High-resolution transmission electron microscopy

The crystal structure of the converted NWs was further studied using TEM. We performed a thorough analysis of three NWs synthesized under the optimal conditions along their entire lengths and found that two of them were entirely single crystalline, and one NW demonstrated partial conversion, forming a Si/ $\text{BaSi}_2$  heterostructure (Fig. S1†). The completely converted NWs were analyzed at multiple locations along the length of the wire, and the crystallinity was verified by obtaining HRTEM micrographs on several spots. A low-magnification TEM image (Fig. 3a) shows a representative  $\text{BaSi}_2$  NW synthesized under the optimal conditions with a diameter of approximately 200 nm, and the inset electron diffraction pattern taken from the entire NW demonstrated only the [331] zone axis, therefore confirming the converted NW to be single crystalline. The HRTEM image (Fig. 3b) shows lattice fringes

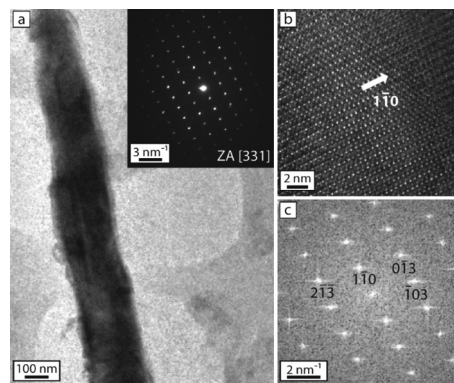


**Fig. 3** TEM micrographs of a representative  $\text{BaSi}_2$  NW synthesized under the optimal conditions. (a) Low-resolution TEM micrograph of a typical NW with inset showing the electron diffraction pattern taken over the entire NW, which confirms the single-crystalline nature of the NW; (b) lattice-resolved HRTEM micrograph along the [331] zone axis and (c) the corresponding indexed FFT pattern.

along the [331] zone axis, confirming the single-crystalline nature of the NW. The two-dimensional fast Fourier transform (FFT) of the lattice-resolved image (Fig. 3c) shows the reciprocal lattice peaks, which can be indexed to the orthorhombic  $\text{BaSi}_2$  lattice (space group  $Pnma$ , with a lattice constant of  $a = 8.92 \text{ \AA}$ ,  $b = 6.75 \text{ \AA}$  and  $c = 11.57 \text{ \AA}$ ).

### Nanostructure control and temperature-independent synthesis of $\text{BaSi}_2$ NW arrays

As mentioned previously, one of the major challenges in conversion reactions is to successfully perform the conversion while preserving the morphology of the initial nanostructures. It is therefore desirable to carry out the conversion at the lowest possible temperature to prevent severe loss of nanoscale morphology. However, in our previous HMS conversion work,<sup>36</sup> we have seen that higher temperature favors the formation of the silicon-rich silicide and lowers the reaction temperature-introduced phase impurities in the products. Therefore, finding the optimal reaction conditions to synthesize the  $\text{BaSi}_2$  NWs described herein required a balance between these requirements. We performed the conversion reaction by placing the initial Si nanostructures at different distances from the center of the furnace and thus different reaction temperatures. We performed separate conversion reactions by placing the Si NWs at 2.2, 3.5 and 4.5 cm downstream from the center of the tube furnace where the alumina boat containing Ba was located (approximate temperatures of 980, 965 and 930 °C, respectively) and analyzed the morphology and phase of the final products after 2 h. The chip placed 2.2 cm downstream (closest to the center of the furnace) showed two distinct regions. The region closer to the center of the furnace looked like a dense film (Fig. 4a), and the region farther away looked like thicker bundles of NWs (Fig. 4b), which clearly showed severe loss of morphology from the initial nanostructures. PXRD patterns of these two regions,



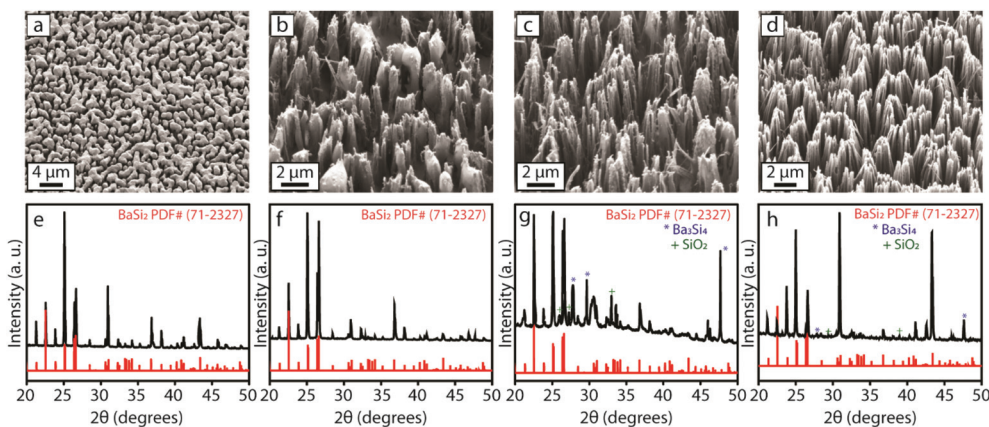


**Fig. 4** Role of the substrate position and reaction temperature on the morphology and phase of the converted nanostructures. SEM images of the final products formed at (a–b) 2.2 cm, (c) 3.5 cm, and (d) 4.5 cm downstream from the center of the furnace (which was set to 1000 °C) and their respective PXRD patterns (e–h), in comparison with the reference diffractogram for BaSi<sub>2</sub> (PDF# 71-2327). The minor Ba<sub>3</sub>Si<sub>4</sub> and SiO<sub>2</sub> impurities are marked by \* and +, respectively.

however, did not reveal any significant differences and indicated that both structures were entirely BaSi<sub>2</sub> phase without any phase impurities (Fig. 4e and f). The products formed at 3.5 cm and 4.5 cm from the center of the furnace retained the initial NW morphology well, as compared to the products at 2.2 cm. In these products, however, some phase impurities in the form of Ba<sub>3</sub>Si<sub>4</sub> and SiO<sub>2</sub> were detectable by PXRD, as shown in Fig. 4g and h. However, these impurities are very minor compared to the major BaSi<sub>2</sub> phase. Additionally, as the temperature decreased, we observed a decrease in the extent of bundling of the NWs, which resulted in a denser array of thinner individual NWs. Based on the morphology of the final product that was at about 930 °C, we take the reaction performed with the chip placed at 4.5 cm downstream from the furnace as the optimized conversion reaction to synthesize BaSi<sub>2</sub> NWs.

It is interesting to note that the substrates placed closer to the center of the furnace showed significant loss of nanoscale morphology as compared to those placed further away from the center. We speculate that the Si NWs placed at higher temperatures (closer to the center) could have a very rapid flux of Ba depositing onto the substrate, which results in the formation of film-like structure. At lower temperatures (further away from the center of the furnace), Ba does not deposit as rapidly but can easily diffuse into the Si NWs, and the nanomorphology is still retained in these structures. It is also worth noting that significant phase impurities arise in the products placed farther away from the center of the furnace (even lower temperatures). This is similar to the HMS conversion work, where several phase impurities were observed at lower reaction temperatures.<sup>36</sup> Furthermore, performing the BaSi<sub>2</sub> conversion reaction for shorter amounts of time at higher temperatures (such as 1000 °C) also gave rise to several impurity phases in the final products (Fig. S2†). These observations suggest that the formation of BaSi<sub>2</sub> could be a phase transformation process where several silicide phases are initially nucleated.

However, at longer reaction times and higher temperatures, due to the higher mobility of Si, the most silicon-rich silicide, *i.e.* BaSi<sub>2</sub>, forms as the eventual product in this system.

#### Optical bandgap and electrochemical measurements

We observed two absorption onsets of ~1 eV and ~1.2 eV in the absorbance spectrum of BaSi<sub>2</sub> NWs (Fig. 5a). Fitting the absorbance spectrum to Tauc plots corresponding to direct and indirect bandgap transitions and further extrapolating the

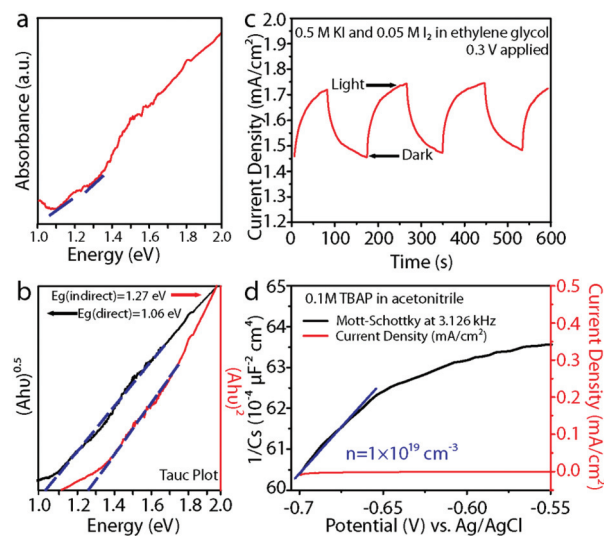


**Fig. 5** Optical and electrochemical properties of the BaSi<sub>2</sub> NW arrays. (a) Absorbance spectrum of the BaSi<sub>2</sub> NW arrays and (b) the corresponding Tauc plots confirming a direct bandgap transition of 1.06 eV and an indirect bandgap transition of 1.27 eV. (c) Photoresponse of BaSi<sub>2</sub> NW arrays under intermittent 1 sun (100 mW cm<sup>-2</sup>) illumination with 0.3 V applied voltage showing a photocurrent of ~0.3 mA cm<sup>-2</sup>. (d) Mott-Schottky analysis of the same NW array showing an n-type carrier concentration of 1 × 10<sup>19</sup> cm<sup>-3</sup>.



linear regions of the fittings, we were able to determine a direct bandgap of 1.06 eV and an indirect bandgap of 1.27 eV for the BaSi<sub>2</sub> NW arrays (Fig. 5b). These observed bandgaps are very close to previously calculated and reported values for BaSi<sub>2</sub> thin films<sup>1,3,42,43</sup> (although there are slight variations on the reported values in the literature). The difference in the morphology (NW vs. thin film) and the fabrication methods could cause slight variations between the reported bandgap values. To further study the electrical properties of the NW arrays, we performed electrochemical measurements of the BaSi<sub>2</sub> NW arrays in the non-aqueous electrolyte ethylene glycol with a KI (0.5 M)/I<sub>2</sub> (0.05 M) redox couple; the corresponding *J*-*V* curves (Fig. S3†) did not show any measureable photovoltage, although the NWs do show a photocurrent response (Fig. 5c), where 1 sun illumination resulted in an increased current of approximately 0.3 mA cm<sup>-2</sup> at an applied voltage of 0.3 V. This observation is very similar to previous reports by several groups of a measurable photocurrent for BaSi<sub>2</sub> film<sup>4,5,44</sup> in solid-state junction devices. It is also worth mentioning that some previous photocurrent measurements of BaSi<sub>2</sub> film on Si substrate reported that even when photoexcited carriers are generated in the BaSi<sub>2</sub> layer, the recombination at the BaSi<sub>2</sub>/Si interface reduces the overall measured photocurrent.<sup>4,44,45</sup> Therefore, it could also be possible that there was some electrical loss at the interface between the BaSi<sub>2</sub> NWs and the underlying Si substrate. Further studies with careful control and tuning of the BaSi<sub>2</sub>/Si interface should be performed to systematically study these interfacial effects on the measurements. To further understand the observed conductivity and to determine the major carrier type of the NW arrays, we performed a Mott-Schottky analysis on the BaSi<sub>2</sub> nanostructures in a solution of 0.1 M TBAP in anhydrous acetonitrile in a three-electrode configuration over the frequency range of 1 Hz to 5 MHz. The resulting Mott-Schottky plot (Fig. 5d) was then generated automatically as the inverse square of the space charge capacitance ( $1/C_S^2$ ) as a function of the applied potential (*V*) using the accompanying Bio-Logic EC-Lab V10.40 software following the classical Mott-Schottky equation:

$$\frac{1}{C_S^2} = \frac{2}{e\epsilon\epsilon_0 N_D} (V - E_{FB})$$

The constants of the Mott-Schottky equation are as follows: electron charge (*e*), the dielectric constant ( $\epsilon$ ), permittivity of free space ( $\epsilon_0$ ), and flat-band potential ( $E_{FB}$ ). Fitting the slope of the Mott-Schottky plot revealed the BaSi<sub>2</sub> NWs to be n-type with a carrier concentration of  $1 \times 10^{19}$  cm<sup>-3</sup>. The observed majority carrier type in our NW array is in agreement with previous reports on BaSi<sub>2</sub> films; however, the reported carrier concentration is approximately 2–3 orders of magnitude larger as compared to previous reports.<sup>1,4,45</sup> We speculate that the difference in carrier concentration could be caused by differences in our sample resulting from the different synthesis methods that yield high surface area nanostructures and the specific precursors that could introduce potential dopants or defects.

## Conclusion

We have used the vapor phase conversion approach to selectively synthesize BaSi<sub>2</sub> NW arrays for the first time by reacting arrays of Si NWs in a CVD tube furnace at 930 °C. We have conclusively characterized the structures, preliminarily examined their optical and electrochemical properties, and provided insights to the conversion mechanism. The NW morphology of the final products can be maintained with optimized reaction conditions, and by changing reaction parameters, BaSi<sub>2</sub> thin films can also be formed. Optical bandgap measurements show that the NWs have direct and indirect bandgap of 1.06 and 1.27 eV, respectively, and preliminary electrochemical measurements suggest that the converted NWs are n-type with a carrier concentration of  $1 \times 10^{19}$  cm<sup>-3</sup>. These properties are very similar to values previously reported for BaSi<sub>2</sub> thin film samples. These novel semiconducting BaSi<sub>2</sub> NWs could be potentially explored for solar energy applications.

## Acknowledgements

This work was supported by a Research Corporation Scialog Collaborative Award for Solar Energy Conversion. L. S. also thanks the support from the NSF Graduate Research Fellowship Program.

## References

- 1 K. Morita, Y. Inomata and T. Suemasu, *Thin Solid Films*, 2006, **508**, 363–366.
- 2 K. Morita, M. Kobayashi and T. Suemasu, *Thin Solid Films*, 2007, **515**, 8216–8218.
- 3 T. Suemasu, *Jpn. J. Appl. Phys.*, 2015, **54**, 07JA01.
- 4 W. Du, M. Baba, K. Toko, K. O. Hara, K. Watanabe, T. Sekiguchi, N. Usami and T. Suemasu, *J. Appl. Phys.*, 2014, **115**, 223701.
- 5 W. Du, R. Takabe, M. Baba, H. Takeuchi, K. O. Hara, K. Toko, N. Usami and T. Suemasu, *Appl. Phys. Lett.*, 2015, **106**, 122104.
- 6 M. J. Bierman and S. Jin, *Energy Environ. Sci.*, 2009, **2**, 1050–1059.
- 7 A. I. Hochbaum and P. Yang, *Chem. Rev.*, 2010, **110**, 527–546.
- 8 T. J. Kempa, R. W. Day, S.-K. Kim, H.-G. Park and C. M. Lieber, *Energy Environ. Sci.*, 2013, **6**, 719–733.
- 9 M. Cabán-Acevedo, D. Liang, K. S. Chew, J. P. DeGrave, N. S. Kaiser and S. Jin, *ACS Nano*, 2013, **7**, 1731–1739.
- 10 M. Pani and A. Palenzona, *J. Alloys Compd.*, 2008, **454**, L1–L2.
- 11 A. L. Schmitt, J. M. Higgins, J. R. Szczech and S. Jin, *J. Mater. Chem.*, 2010, **20**, 223–235.
- 12 A. L. Schmitt, M. J. Bierman, D. Schmeisser, F. J. Himpsel and S. Jin, *Nano Lett.*, 2006, **6**, 1617–1621.
- 13 A. L. Schmitt, L. Zhu, D. Schmeisser, F. J. Himpsel and S. Jin, *J. Phys. Chem. B*, 2006, **110**, 18142–18146.



- 14 Y.-H. Liang, S.-Y. Yu, C.-L. Hsin, C.-W. Huang and W.-W. Wu, *J. Appl. Phys.*, 2011, **110**, 074302.
- 15 A. L. Schmitt, J. M. Higgins and S. Jin, *Nano Lett.*, 2008, **8**, 810–815.
- 16 J. M. Higgins, P. Carmichael, A. L. Schmitt, S. Lee, J. P. Degrave and S. Jin, *ACS Nano*, 2011, **5**, 3268–3277.
- 17 J. M. Higgins, R. Ding, J. P. DeGrave and S. Jin, *Nano Lett.*, 2010, **10**, 1605–1610.
- 18 J. M. Higgins, R. Ding and S. Jin, *Chem. Mater.*, 2011, **23**, 3848–3853.
- 19 J. M. Higgins, A. L. Schmitt, I. A. Guzei and S. Jin, *J. Am. Chem. Soc.*, 2008, **130**, 16086–16094.
- 20 J. R. Szczech, A. L. Schmitt, M. J. Bierman and S. Jin, *Chem. Mater.*, 2007, **19**, 3238–3243.
- 21 Y. Song, A. L. Schmitt and S. Jin, *Nano Lett.*, 2007, **7**, 965–969.
- 22 Y. Song and S. Jin, *Appl. Phys. Lett.*, 2007, **90**, 173122.
- 23 Y. Wu, J. Xiang, C. Yang, W. Lu and C. M. Lieber, *Nature*, 2004, **430**, 61–65.
- 24 Y. Chen, Y.-C. Lin, C.-W. Huang, C.-W. Wang, L.-J. Chen, W.-W. Wu and Y. Huang, *Nano Lett.*, 2012, **12**, 3115–3120.
- 25 Y. Chen, Y.-C. Lin, X. Zhong, H.-C. Cheng, X. Duan and Y. Huang, *Nano Lett.*, 2013, **13**, 3703–3708.
- 26 W.-L. Chiu, C.-H. Chiu, J.-Y. Chen, C.-W. Huang, Y.-T. Huang, K.-C. Lu, C.-L. Hsin, P.-H. Yeh and W.-W. Wu, *Nanoscale Res. Lett.*, 2013, **8**, 290.
- 27 K.-C. Lu, W.-W. Wu, H.-W. Wu, C. M. Tanner, J. P. Chang, L. J. Chen and K. N. Tu, *Nano Lett.*, 2007, **7**, 2389–2394.
- 28 K. Yamamoto, H. Kohno, S. Takeda and S. Ichikawa, *Appl. Phys. Lett.*, 2006, **89**, 083107.
- 29 Y.-C. Lin, K.-C. Lu, W.-W. Wu, J. Bai, L. J. Chen, K. N. Tu and Y. Huang, *Nano Lett.*, 2008, **8**, 913–918.
- 30 B. Liu, Y. Wang, S. Dilts, T. S. Mayer and S. E. Mohny, *Nano Lett.*, 2007, **7**, 818–824.
- 31 K.-C. Lu, W.-W. Wu, H. Ouyang, Y.-C. Lin, Y. Huang, C.-W. Wang, Z.-W. Wu, C.-W. Huang, L. J. Chen and K. N. Tu, *Nano Lett.*, 2011, **11**, 2753–2758.
- 32 H.-B.-R. Lee, G. H. Gu, C. G. Park and H. Kim, *J. Electrochem. Soc.*, 2012, **159**, K146–K151.
- 33 Y.-C. Lin, Y. Chen, R. Chen, K. Ghosh, Q. Xiong and Y. Huang, *Nano Lett.*, 2012, **12**, 4341–4348.
- 34 Y.-C. Lin, Y. Chen, A. Shailos and Y. Huang, *Nano Lett.*, 2010, **10**, 2281–2287.
- 35 Y.-H. Hsieh, C.-H. Chiu, C.-W. Huang, J.-Y. Chen, W.-J. Lin and W.-W. Wu, *Nanoscale*, 2015, **7**, 1776–1781.
- 36 A. Pokhrel, Z. P. Degregorio, J. M. Higgins, S. N. Girard and S. Jin, *Chem. Mater.*, 2013, **25**, 632–638.
- 37 L.-W. Chu, C.-W. Hung, C. Y. Wang, Y.-H. Chen, J. Tang, K. L. Wang and L.-J. Chen, *J. Electrochem. Soc.*, 2011, **15**, K64–K68.
- 38 H. Liu, G. She, X. Huang, X. Qi, L. Mu, X. Meng and W. Shi, *J. Phys. Chem. C*, 2013, **117**, 2377–2381.
- 39 Y. Kang and S. Vaddiraju, *Chem. Mater.*, 2014, **26**, 2814–2819.
- 40 S. Lee, J. Yoon, B. Koo, D. H. Shin, J. H. Koo, C. J. Lee, Y.-W. Kim, H. Kim and T. Lee, *IEEE Trans. Nanotechnol.*, 2013, **12**, 704–711.
- 41 K. Peng, Y. Yan, S. Gao and J. Zhu, *Adv. Funct. Mater.*, 2003, **13**, 127–132.
- 42 T. Nakamura, T. Suemasu, K.-i. Takakura, F. Hasegawa, A. Wakahara and M. Imai, *Appl. Phys. Lett.*, 2002, **81**, 1032–1034.
- 43 Y. Matsumoto, D. Tsukada, R. Sasaki, M. Takeishi and T. Suemasu, *Appl. Phys. Express*, 2009, **2**, 021101.
- 44 T. Suemasu, T. Saito, K. Toh, A. Okada and M. A. Khan, *Thin Solid Films*, 2011, **519**, 8501–8504.
- 45 K. O. Hara, N. Usami, K. Toh, M. Baba, K. Toko and T. Suemasu, *J. Appl. Phys.*, 2012, **112**, 083108.

